MICROCOPY RESOLUTION TEST CHART

ed for Public Release:
bution Unlimited

NEPEF Technical Report 7-77 (CDC)

DTIC
ELECTE
APR 0 3 1986
S D

EVALUATION OF OBJECTIVE PARAMETERS

DERIVED FROM CONCENTRIC CLOUD PATTERNS

By

D. G. Dartt
Research Division
Control Data Corporation
Minneapolis, MN 55440

For

Naval Environmental Prediction Research Facility
U. S. Navy
Monterey, CA 93940

30 June 1977

86 4 1 142

DISCLAIMER NOTICE

**THIS DOCUMENT IS BEST QUALITY
PRACTICABLE. THE COPY FURNISHED
TO DTIC CONTAINED A SIGNIFICANT
NUMBER OF PAGES WHICH DO NOT
REPRODUCE LEGIBLY.**

TABLE OF CONTENTS

I.   INTRODUCTION

In previous studies, Dartt, et al. (1974), Dartt (1975, 1976), computer programs have been developed to monitor the position, intensity, and rotation of cyclones from digital satellite cloud patterns. The current effort provides a test of these algorithms from a large sample of tropical and extra-tropical storms. The technique is based on finding the distribution of centers of curvature from elements of concentric cloud bands surrounding the storm. The location of the maximum of this distribution is the focal point of the cloud bands and is defined as the storm center. Other parameters computed from this distribution yield objective measures of storm concentricity and rotation.

A primary use of the algorithms is to monitor cyclonic vortices from the high volume of image data available from geosynchronous and orbiting satellites. The programs can be used to follow the process of storm development over the oceans where few conventional meteorological observations are available. In particular, any site which has the capability to receive satellite data and has computer resources can monitor characteristic features of storms in its vicinity.

Most emphasis in this investigation has been placed on the analysis of tropical storms. Current operational techniques of monitoring tropical storms include aircraft reconnaissance and satellite photo interpretation by experienced analysts. The technique of Dvorak (1975) of interpreting the minimum surface pressure of the storm and the maximum wind from the concentric cloud patterns is particularly useful for estimating extreme weather variations. Also, Fett and Brand (1975) have analyzed the rotation of storms with respect to changes in the storm's trajectory. The investigation conducted here is to provide tools for the support of these efforts. For example, in this report a method is described for obtaining objective Dvorak T-numbers from visual and infrared (IR) satellite images in order to monitor the storm continuously over a 24-hour period. Also, a reference axis is defined from which to measure storm rotation with time.

For extra-tropical storms, the relationships of cloud parameters are analyzed with respect to position and movement of the storm as seen from a satellite. An attempt is made to relate the concentricity of the storm to

the amplitude of the respective shortwave trough at 500 mb. Nagle and Hayden (1971) have found good relationships between cloud parameters and shortwave troughs at this altitude. Similarly, Troup and Streton (1972) have classified cloud patterns of extra-tropical storms in order to initialize upper-air height fields in data sparse regions of the southern hemisphere.

Accesion For

NTIS	CRA&I	☑
DTIC	TAB	☐
Unannounced		☐
Justification		

By *lta..on file*

Distribution /

Availability Codes

Dist	Avail and / or Special
A-1	23

2

II. CALCULATION OF THE CENTER OF CURVATURE DISTRIBUTION

A. TECHNIQUE

The procedure for computing the center of curvature distribution of spiral cloud bands has been described in detail in previous reports (Dartt et al., 1974, and Dartt, 1975). It is repeated here with emphasis on user application to both tropical and extra-tropical storms.

The first requirement is to have an image of a cyclonic cloud pattern in digital form. Visual or IR images can be analyzed using picture elements of 6-bit precision (0-63) in gray scale. The image should be scaled so that the cloud bands have larger values than the underlying sea surface. IR images do not need to be converted to temperature before computer analysis.

The basic image array consists of 128x128=16384 (40000 octal) elements. This is as large an array as is practical to analyze on a general purpose computer in batch processing mode. (For a 128x128 array, the program storage is approximately 140000 octal locations.) It is important to retain as much image resolution as possible but still contain the entire storm in the 128x128 array. For tropical storms, an image resolution of 11 km was used in this study. For extra-tropical storms, an image resolution of 22 km was used so that the primary cloud vortex along with the frontal cloud band could be contained in the image array. Note: Changing the image resolution results in non-linear changes in parameters derived from the center of curvature distribution, and thus parameters derived from different resolution data cannot be compared.

For tropical storms, the tentative storm center of the image should be located near the center of the 128x128 array, Figure 1, so that concentric bands near the perimeter of the storm can contribute to the center of curvature distribution. For extra-tropical storms in the northern hemisphere, the cloud vortex should be displaced to the left and upwards from the center of the image array so that the leading edge of the frontal cloud band occurs within the image array (see Figure 17).

Step 1. In the first computation step, a digital filter is used to enhance the banded concentric cloud structure of the storm. The wave number response function, $S(k_x, k_y)$, of the filter is Gaussian in form and radially

3

symmetrical about $k_x = k_y = 0$.

$$S(k_x, k_y) = \exp \{-(k_r - F_m)^2/\sigma^2\}$$

$$k_r = \{k_x^2 + k_y^2\}^{\frac{1}{2}} \qquad (1)$$

Here k_x and k_y are wave numbers in the x and y direction, k_r is a comparable radial wave number, F_m is the radial wave number of maximum response, and σ is a parameter controlling the width of the response function. F_m and σ are chosen by the analyst to enhance the banded structure of any desired scale. After considerable experimentation with both tropical (40 images) and extra-tropical (11 images) storms, the filter parameters $F_m=22$ and $\sigma=8$ were chosen to be optimum for producing distinctive center of curvature distributions. The peak filter response, F_m, for 11 km resolution tropical images is at a wavelength of 64 km. For 22 km resolution extra-tropical images, the peak filter response occurs at a wavelength of 128 km. The IR cloud pattern and filter pattern for the western Pacific Tropical Storm Gilda, July 04, 1974, 1226Z, are shown in Figures 1 and 2, respectively.

Step 2. In the second computation step, a skeleton of the filtered bands is computed to compress the filter pattern to a new standard line segment form. The orientation of the original banded structure is preserved as seen in Figure 3. The edges and corners of the filter pattern are discarded because of an undesirable halo sometimes produced at the image boundary.

Step 3. The angular orientation of short line segments of the skeleton cloud band pattern is now computed. This is done by correlating a rectangular mask of specific orientation with the skeleton pattern. The mask is designed to select narrow line segments of fixed angular direction and inhibit line segments oriented in other directions. Repeated applications of this mask for various angles comprising a 360° circle generates a complete angular analysis of the segmented cloud band pattern.

Step 4. Rays are constructed which are orthogonal to the directions of the skeleton segments from the angular analysis above. The length of the rays is 41 grid elements on either side of the midpoint of the skeleton segment. For concentric cloud bands, the rays converge towards the center of curvature

4

and diverge on the opposite (convex) side of the bands. The resulting
pattern of converging rays from all concentric cloud band segments produces
a composite center of curvature distribution for the entire storm system.
This distribution is defined as the number of rays per cell within the super-
imposed 128x128 cellular grid. At this stage, the computer has analyzed the
pattern in much the same way as a human analyst, i.e., concentric cloud bands
have been selected, and the center of curvature distribution for segments of
these bands has been described.

Step 5. A normalization of the center of curvature distribution is now
performed so that the final pattern primarily indicates concentricity and is
not a function of the number of cloud band segments. If Steps 2, 3, and 4
are applied to a pattern of cloud bands with random orientation, the computed
center of curvature will correspond to the center of gravity of the pattern.
To estimate the random pattern, a separate center of curvature distribution
is computed based on the same distribution of skeleton segments as before.
However, a random orientation of each segment is assumed rather than the
specific orientation found earlier. The resulting pattern based on the sum of
the random components associated with all skeleton segments is then subtrac-
ted from the original center of curvature pattern to produce the "normalized"
pattern. The normalization produces a positive pattern on the concave side
of a cloud band and negative pattern on the convex side of this band. Only
the positive portion of the normalized center of curvature pattern is saved
for the remainder of the analysis. An example of the normalized center of
curvature distribution for the IR cloud pattern of Gilda on July 04, 1974,
is shown in Figure 4.

Characteristically, the normalization may produce some noisy patterns
in the corners of the 128x128 grid. Any cloud bands which are concave with
respect to the grid corners will produce a residual center of curvature
pattern there. In Step 2, the cloud bands in the corners are removed from
analysis, and the random pattern in the corners is therefore always small.
Thus, the normalized distribution of centers of curvature in the grid corners
is larger than would have occurred had the corner grid points been retained.

5

B. OBJECTIVE PARAMETERS

Various objective parameters of the normalized center of curvature distribution are useful for analysis of storm characteristics.

1. <u>Locating the center of the storm</u>. The grid cell with the maximum number of intersecting rays is the focal point of the concentric cloud bands and is defined as the storm center.

2. <u>Measure of storm concentricity related to storm intensity</u>. The magnitude of the center of curvature distribution is found by integrating the distribution in a circular region about the storm focal point given above. This magnitude is the average density of rays throughout the circular area and is called the d (density)-number . The d-number is an objective measure of concentricity of the storm as indicated by curvature in the cloud bands.

3. <u>Reference axis for measuring storm rotation</u>. The major axis of the ellipse used to characterize the two dimensional center of curvature distribution is a parameter indicating an axis of curvature for the cloud bands which can be monitored with time from successive images. The angle of the major axis (γ) with respect to the coordinate axes is defined by:

$$2\gamma = \tan^{-1} \frac{2r_{xy}s_x s_y}{s_x^2 - s_y^2} \tag{2}$$

where s_x and s_y are the respective standard deviations of the center of curvature distribution in the east-west and north-south directions, and r_{xy} is the correlation of this distribution between the x and y directions. The major axis is defined from the same area of the center of curvature distribution surrounding the storm focal point used to compute the d-number. The major axis is indicated by a straight line in the accompanying center of curvature distribution (Figure 4).

4. <u>Storm ellipticity</u>. To measure the storm's elliptical characteristic, the ratio of standard deviations along the major (σ_a) and minor (σ_b) axes of the ellipse characterizing the center of curvature distribution is calculated. This parameter is useful for estimating the error of position of extra-tropical storms as given in IV-C-3.

6

III. TROPICAL STORM ANALYSIS

A. OBJECTIVE

Parameters of the center of curvature distribution of cloud bands for tropical storms in the western Pacific are evaluated for analyzing the storm's intensity (d-number), rotation (major axis), and position (location of maximum).

B. DATA

Film images of tropical storms were obtained from the DMSP satellite film library at the University of Wisconsin, Madison. Samples of IR and visual images of selected typhoons were chosen that characterized the growth cycle of tropical storms. All storms selected had histories of intensity and position in the Annual Typhoon Reports published by the Joint Typhoon Warning Center in Guam. The films were digitized with an Optronics P-1000 Photoscanner which produced a basic 500x500 image array of 3 km resolution. (The calibration of the Photoscanner was not changed during the scanning of all storm images.) The final 128x128 image array of 11 km resolution used for computation was derived from this higher resolution array. Table 1 shows the storm images chosen for analysis.

TABLE 1. Tropical storm images used for concentricity analysis

	Number of Images		
Tropical Storm	Visual	IR Normal	IR Inverse
Nora, Oct 3-10, 1973	6	-	6
Patsy, Oct 7-11, 1973	4	-	7
Gilda, Jun 26-Jul 7, 1974	8	6	-
Mary, Aug 11-24, 1974	8	4	1
Polly, Aug 23-31, 1974	6	10	-
Rose, Aug 27-31, 1974	4	4	-
Shirley, Sep 4-8, 1974	3	4	2

The DMSP typhoon images originally came from various tactical sites in the western Pacific (Guam, Fuchu, Kadena, and Nakhon Phanom). Each site has its characteristic method of displaying IR data. In the normal mode, clouds

7

appear dark against a lighter background sea surface. In the inverse mode, clouds appear white against a darker sea surface. All IR inverse mode images except one came from Fuchu. For an unknown reason, the Fuchu IR images all have a narrower range of IR brightness variability than the IR images from other sites. Figure 5 shows two IR images of Typhoon Shirley recorded within a few seconds of one another by the same sensor (2.4 nautical mile [n.mi.] resolution IR). The image from Guam is 6-bit IR data in the normal mode but has been inverted (brightness elements have been subtracted from 63) so the clouds appear white in the usual meteorological sense. The second image is 6-bit image data from Fuchu, IR inverse mode. The graph below the images indicates the brightness distribution of the two images. Here, the brightness is also expressed as temperature using the linear conversion described in the DMSP User Guide (1974). For September, the sea surface temperature in this region is approximately $301^{\circ}K$. According to the DMSP User Guide, the 2.4 n.mi. resolution IR sensor typically underestimates the sea surface temperature by $5-10^{\circ}K$ in the tropics, depending on viewing angle. Thus, the image temperature distribution from Guam appears physically more reasonable than that for Fuchu.

The concentricity analysis based on filtered cloud patterns is largely a function of spatial variations in the brightness field so differences in calibration of the two images do not significantly effect the d-number. However, in the storm intensity classification described below, it is necessary to define a measure of area cloudiness that is dependent on an IR brightness (temperature) threshold. Each type of image has a different temperature range for its gray scales, and different gray scale resolution, but it should be possible to compare absolute cloud temperatures. However, in practice, this is not the case as explained later.

The IR image sample in Table 1 contains a few images based on the DMSP .33 n.mi. resolution sensor in addition to the images based on the 2.4 n.mi. resolution sensor. The DMSP User Guide indicates that the high resolution sensor underestimates temperatures by $20^{\circ}K$ compared to the low resolution sensor. Thus, when the .33 n.mi. data are used to determine area cloudiness, the $20^{\circ}K$ correction is applied.

All of the above problems in image and sensor calibration could be avoided if a set of precalibrated digital data were available. Because of the high volume of DMSP data, a general archive of all digital data is not feasible. However, for such phenomena as tropical storms, such an archive may be practical.

C. RESULTS

1. Typhoon intensity classification. The Dvorak technique of classifying tropical storms from satellite cloud patterns is based on an analyst's interpretation of storm concentricity and the area of central dense overcast cloudiness. The d-number defined from the distribution of centers of curvature of the storm is an objective measure of concentricity. An investigation was undertaken to see if it could be useful for objective storm intensity classification.

Initially, d-numbers were computed from images of three storms (Nora, Gilda, and Mary) and compared to Dvorak T-numbers available in the Annual Typhoon Reports. These storms were quite different in their cloud and intensity characteristics. Nora was a super-storm with winds greater than 135 knots and a massive central cloud mass which had few concentric bands other than a well defined eye, Figure 6a. Gilda was a tropical storm of moderate intensity and well defined concentricity, Figure 1. Mary was a weaker storm with moderate concentricity, Figure 6b. Preliminary analysis of these storms indicated that large amounts of high level clouds often obscurred the concentric banding of lower level clouds. Typically, in the growth cycle of the storm, the concentricity as given by the d-number might be moderate (1.0-2.0) in the early stages of storm development, followed by a decrease (0.5-1.5) as large amounts of high cloud were generated by the storm. As the storm reached its peak intensity and began to dissipate, the concentricity increased again and reached its largest value (2.0-5.0). Thus, it became apparent that an additional variable based on image cloudiness would have to be included with the d-number to account for the primary storm intensity variability. Since both the area of cloud overcast and concentricity are proportional to storm intensity in the Dvorak technique, it was decided to formulate a simple linear model of storm intensity according to:

9

$$T = a \bullet (\text{d-number}) + b \bullet (\text{percentage image covered by cold cloud}) \quad (3)$$

where T is the storm intensity as given by the Dvorak T-number and a and b are regression coefficients (weights) to be found from a sample of d-numbers and area of cloudiness calculated from satellite typhoon images in Table 1.

To determine the statistical model, the percentage of the image colder than a threshold temperature, T_o (where $T_o = 220$, 230, $\ldots$, $290^{\circ}K$), was calculated for IR images from Typhoons Gilda and Mary. One IR image from Typhoon Nora was also included based on data from Nakhon Phanom that did not indicate the calibration problems of the Fuchu images. A total of 11 images was used to define the model. Separate models were formulated for d-numbers derived from visual and IR images, although in both models the cloudiness parameter is based on the IR image. The T-numbers used for model development came from the Annual Typhoon Report. For a given satellite image, different T-numbers can occur because of the interpretation of the cloud pattern by different analysts. The average of individual T-numbers was used for T-number input for model development and also for later model verification.

Figure 7 indicates the residual error of both IR and visual models as a function of the temperature threshold, T_o. At a threshold temperature of $T_o = 270^{\circ}$ (based on IR normal films), the error of both models is near minimum with a standard deviation of approximately two-thirds of a T-number. This residual error is larger than the variation of T-numbers by photo-analysts as described by Sheets and Grieman (1975). To reduce the error further requires additional terms in the model which are not practical to formulate at this time because of the limited data sample. For the threshold temperature of 270°, $a = .5615$ and $b = .0564$ for IR images; while $a = .4995$ and $b = .0639$ for visual images. (The units of a are T-number/d-number and for b the units are T-number.)

Figure 8 indicates the T-numbers of the model for Typhoon Gilda formulated with Equation 3 and the optimized regression coefficients a and b given above. The individual contributions to the T-numbers by the concentricity and cloud area terms are also indicated. The cloud area appears more important than the concentricity, although the latter's importance increases with storm maturity. It can be seen that both the visual and IR

10

d-numbers jointly produce an internally consistent set of model values whose envelope describes the primary time variability of observed T-numbers. In Figure 8, the dropsonde surface pressure from air reconnaissance flights is also indicated as a direct measure of a storm intensity. Tables showing the inverse relationship between the minimum sea level pressure and satellite T-numbers are given in Dvorak (1975).

To verify the model, the coefficients a and b derived from the previously described 11 images are applied to the IR and visual images from Typhoons Polly, Rose, and Shirley. Practically all IR images from these typhoons are in the normal mode and, therefore, consistent with the IR images used to define the model.

Polly was a tropical storm of moderate intensity (maximum winds, 95 knots) and good concentricity in its mature stage, Figure 9. The model and observed T-numbers are shown in Figure 10 for this storm. The envelope of T-numbers of the model describes the primary storm variations quite well, and there is internal consistency between T-numbers based on visual and IR image data. As in the case of Gilda, Figure 8, the d-number contributes significantly to the T-number during the storm's mature and dissipating stages. On a systematic basis, the model appears to underestimate the observed T-number in the dissipating stage (after August 29) by approximately 1 to 1.5 T-numbers.

Tropical Storms Rose and Shirley are distinctly weaker storms whose model and observed T-numbers are given in Figure 11. Rose, Figure 9b, and Polly were a binary storm pair occuring in the same general region; Shirley, Figure 5, occurred a few days later in this same area. The model T-numbers for Tropical Storm Rose are within approximately $\pm .5$ T-numbers of the subjective values. These values for Shirley systematically underestimate the observed values by about 1 T-number up to the time of maximum storm development.

The verification statistics for Polly, Rose, and Shirley are given in Table 2.

11

TABLE 2. Difference (D), modeled minus observed T-numbers

Parameter	IR Images	Visible Images
Average D	-.6	-.4
RMS D	1.0	.9
$\left[\overline{D^2} - (\overline{D})^2\right]^{\frac{1}{2}}$	.6	.8
Number of images	17	11

The model-derived T-numbers appear too small by approximately one-half T-number for both IR and visual images. Further, the RMS difference between modeled and observed T-numbers is about ± 1 T-number. If the negative bias between modeled and observed values is removed, the resultant residual error, Table 2-row 3, is very nearly the same as the residual error of the original model, Figure 7.

There are two sources of error in the subjective analysis of T-numbers. One is the variation of T-numbers as a function of analyst, the other is the error of approximating the minimum sea level pressure and maximum wind speed from the T-number. In this investigation, we have not been concerned with the latter error, but rather with developing a model that synthesizes the average T-number of various analysts. Sheets and Grieman (1975) indicated that 60 to 90 percent of T-numbers produced by analysts from DMSP images are within $\pm .5$ of an official "best" T-number. The range reflects various analysis groups and storm severity classifications. Further, 85 to 100 percent of T-numbers produced by analysts from this data source are within ± 1 of the official T-number, and 94 to 100 percent within ± 1.5 of this number. Here, 10/28 or 36 percent of the comparable differences between modeled and averaged subjective T-numbers lie within $\pm .5$, 18/28 or 64 percent within ± 1.0, and 26/28 or 93 percent within ± 1.5. Clearly, the statistical model described here based on only eleven storm images does not have the accuracy of the human analyst.

To model T-numbers from the IR inverse images for Typhoons Nora and Patsy (Fuchu images), a calibration of the IR brightness difference between images in the normal and inverse modes must be devised. This was done using the two IR brightness distributions of the same image of Typhoon Shirley

12

shown in Figure 5. The threshold temperature of clouds on which the model was based was $270^{\circ}K$ for the IR normal image. Using this threshold temperature, the percentage cloud was computed for the IR normal image from Guam. For the IR inverse Fuchu image, a new threshold temperature was found which gave the same percentage of cloud as the previous image. This temperature was $238^{\circ}K$ as indicated on the temperature distribution of the IR inverse image, Figure 5. The threshold temperature $238^{\circ}K$ was then used with the remaining images of Typhoons Nora and Patsy to define the percentage cloudiness to be used with the previous derived regression coefficients.

Figure 12 shows the observed and model T-numbers for these two storms. The model underestimates the T-number at the time of the storm maximum by as much as two T-numbers for Patsy, primarily because of lack of concentricity of the cloud patterns. Patsy and Nora were superstorms whose very cold cirrus shields were extensive and obscured the concentricity of lower levels. The DMSP IR sensor does not respond to temperatures below $210^{\circ}K$, and the entire cloud area of these storms was devoid of features in the IR images. In these storms, distinctive diurnal variations of modeled T-numbers are evident as a result of diurnal variations in cloud area. The nighttime T-numbers for Patsy (10/07/12Z, 10/08/12Z) and Nora (10/05/12Z, 10/09/12Z) show distinctive minima compared to those computed at midday. Diurnal variations also trouble the subjective interpretation of storm intensity (Dvorak, 1975).

Because of the tentative nature of calibration of these IR inverse images, these cases were not included with the previous verification. The average difference of modeled minus observed T-numbers is -.7 for the IR images and -.2 for the visual images indicating a systematic underestimate of modeled T-number as occurred in the previous verification based on IR normal images. Only 4/23 or 17 percent of the modeled-observed differences are within $\pm.5$ T-numbers, 11/23 or 48 percent within ±1.0, and 16/23 or 70 percent within ±1.5. This degradation in model accuracy from the IR normal images probably reflects the calibration problems between the two film types.

Clearly, at this stage of the development, the statistical model does not reflect the accuracy of existing subjective techniques. However, there is

13

significant evidence of skill as shown by the ability to describe relative intensity changes. No doubt better results could be obtained with a pre-calibrated set of digital data than with the digital films that were analyzed here. Further, there is evidence of systematic departures in the model that may be corrected with additional terms. Notable is the negative bias which could be corrected by a constant term. Also, a tendency to underestimate the strength of storms at maturity probably could be corrected by including a second cloud variable indicating the area of high clouds or by adding a higher polynomial of concentricity such as the square of the d-number.

2. <u>Rotation of major axis</u>. The major axis of the center of curvature distribution is a reference line that can be monitored for storm rotation, and it is compared to direction changes of the storm along its trajectory. Figure 13 indicates the major axis of curvature of visual and IR images superimposed on the official storm track of Typhoon Mary (Annual Typhoon Report, 1974). For this storm, the major axes derived from both visual and IR images are nearly parallel to the storm track for the complete trajectory of the typhoon. Figure 14 shows a similar diagram for Typhoon Gilda. Here the major axis is not oriented parallel to the storm track. Still, changes in the storm's trajectory are reflected by the behavior of the major axis. For example, between July 1 and July 4, the axis is noted to rotate anticyclonically corresponding to similar changes in the storm's trajectory. The difference between the major axis of visual and IR images as seen in Figure 14 is somewhat typical of most storms. The IR image axis is usually not the same as the axis computed from the visual image; however, both axes generally show similar time behavior along the storm's trajectory. Figure 15 indicates the major axes of the IR images for Typhoon Polly and Tropical Storm Rose. Rose initially occurred to the west of Polly and was moving northeastward. On August 30, Rose was strongly influenced by Polly's circulation and began to move rapidly around the southern flank of this larger storm. Polly may also have been influenced by Rose as Polly's trajectory indicates considerable cyclonic curvature at this time. The major axis of Polly indicates consistent anticyclonic rotation from August 24 to September 1. There are two large-scale anticyclonic deflections in the storm track on August 26 and August 31. (Note, the inset on Figure 15 indicates

14

that the deflection on August 26 may have been cyclonic with a rotation greater than 360°.) Both direction changes occur when the storm's speed is small (parameter A on diagram). The anticyclonic rotation of the major axis may be a predictor of these direction changes. When the storm's speed is large, such as when it is being advected by a predominant large-scale flow pattern, the rotation of the major axis may not be important.

The major axis analysis for Typhoon Shirley is not shown here but its pattern was not unlike that for Typhoon Gilda where rotational changes in the axis appeared to occur concurrently with directional changes in the storm trajectory. Two storms, Nora and Patsy, had very poor center of curvature distributions because extensive amounts of cold clouds obscured the concentric banding. For these storms, the major axis did not appear related to the storm track.

In conclusion, the behavior of the concentricity axis of the storm appears to reflect changes in the storm's trajectory at least for storms of moderate intensity. In one storm, Polly, the rotation appeared to precede the subsequent direction changes. For the remaining storms, the rotation changes in the storms' axis appeared to occur concurrently with similar direction changes in the storm trajectory and, therefore, did not seem to have any significant predictive value. As a result, the major axis appears most useful for monitoring current direction changes of the storm and perhaps extrapolating them into the near future. Also, the major axis may be useful for helping to diagnose direction changes of storms where the steering flow is not well defined.

3. Locating the storm center. In an earlier study, Dartt, et al. (1974), the location of the maximum value in the distribution of centers of curvature was compared to a subjective interpretation of the storm center for a small number of tropical storm visual images. Here a similar comparison is made for the large number of visual and IR images used in this study, Table 3.

TABLE 3. Cumulative distribution of the distance apart
of objective and subjective centers of tropical storms

Image	Number	Distance apart in 11 km grid units											
		0-3	0-6	0-9	0-12	0-15	0-18	0-21	0-24	0-27	0-30	0-33	0-36
IR	45	27	44	51	62	73	80	84	84	89	93	96	100%
Visual	38	32	47	63	71	82	84	89	92	95	97	97	100%

The center can be found more accurately from the visual than the IR images. This is because the cloud tops of many of the most intense storms are so cold as to not exhibit any concentric bands as measured by the IR sensor on the DMSP satellite.

Sheets and Grieman (1975) discuss the analyst's error of storm position from the "best satellite track". For DMSP data, 33 percent of the cases were within 20 n.mi. (37 km) of the optimum location, 76 percent were within 40 n.mi. (74 km), and 91 percent were within 60 n.mi. (111 km). Thus, from a comparison of the values in Table 3 the subjective storm centers appear more accurate than the objective centers found here. This presumes that the subjective position used for comparison with the objective storm fix occurs along the "best satellite track". The subjective analyses are based on the very high resolution visual data (.6 km) of the DMSP satellite, while the objective technique uses data of 11 km resolution. The accuracy of the objective technique improves with higher resolution data. In the current analysis, the 11 km resolution data were necessary for the storm intensity model described earlier.

The difference between objective and subjective storm positions was also analyzed as a function of the d-number and storm ellipticity (II-B-4). For storms whose d-number was less than 1.25, the mean position difference was 12 grid increments (40 cases). For d-numbers between 1.25 and 2.50, the mean position difference was 11 grid increments (23 cases), and for storms with d-numbers greater than 2.5, the position difference was only 2 grid increments (16 cases). Thus, storms with good concentricity can be

positioned very accurately. There did not seem to be any relation between objective-subjective position difference and storm ellipticity.

IV. EXTRA-TROPICAL STORM ANALYSIS

A. OBJECTIVE

Parameters from the distribution of centers of curvature of cyclonic cloud patterns are analyzed for the purpose of calculating the position, intensity, and movement of extra-tropical storms. The storms analyzed are upper level vortices that typically have well-defined spiral cloud patterns. Such cloud vortices are well correlated with features of the 500 mb geopotential height pattern (Nagle and Hayden, 1971).

B. DATA

Cloud concentricity patterns are computed from satellite IR images of NOAA-4. Data for two periods, February 27 - March 5, 1975, and March 26 - April 5, 1976, are analyzed for both the Atlantic and Pacific oceans. The procedure was to follow a given storm through its growth stages and compute the respective parameters of the cloud patterns. A total of 33 images for five storms in the Pacific and 26 images for five storms in the Atlantic were analyzed. In the Pacific, two storms occurred off the east coast of Japan and three of the west coast of California. In the Atlantic, one storm was a weak subtropical vortex and the remaining storms traversed the ocean at higher latitudes.

Figures 16 and 17 show one of the extra-tropical storms in the western Pacific at successive 12-hour intervals. The distribution of the centers of curvature evolve in much the same way as for a tropical storm, and for this storm the intensity given by the d-number attains the large values that are characteristic of the tropics. Typically the center of curvature distribution for extra-tropical storms is more elongated than circular as a result of the comma-shaped cloud pattern associated with the frontal band.

C. RESULTS

1. <u>Comparison of d-number and 500 mb trough magnitude</u>. The hypothesis was made that concentricity in the cloud patterns as measured by the d-number is correlated to geostrophic vorticity (ζ_g) computed from the geopotential height field (z);

18

$$\zeta_g = (g/f)\nabla^2 z$$

$$f = 2\Omega \sin\Theta \qquad\qquad (4)$$

where g is the gravitational constant and f is the Coriolis parameter derived from the rotation rate of the earth (Ω) and latitude (Θ). The Laplacian of a scalar field is a measure of the departure of a local value from the surrounding regional average. Thus, the geostrophic vorticity is well correlated with the shortwave portion of the original height field. As a result, the product of the d-number and $\sin\Theta$ should be correlated with the amplitude of the shortwave trough. The amplitude of the shortwave trough was computed by application of the Holl (1963) scale analysis program to NEPRF grid data for 12-hour periods corresponding to the intervals of satellite images. This program partitions the variability of the height field into long and short wave components. The spectral characteristics of the shortwave component are controlled by a parameter α. For this study $\alpha=5$, and the amplitude of waves shorter than five grid lengths (one grid length is 361 km) are unchanged by the analysis. However, waves larger than 24 grid lengths are completely removed, and the amplitude of waves of 11 grid lengths is reduced by 50%.

As a first test, five possible cloud predictor variables were correlated with the amplitude of the 500 mb shortwave trough. These included latitude, Θ, cloud diameter, D, cloud amplitude, A, concentricity, $d \cdot \sin\Theta$, and percentage area cloudiness, C, where C is defined as the fraction of the IR temperature pattern colder than a given threshold T_0. Nagle and Hayden (1971) found the first three variables to have significant correlation with the 500 mb shortwave pattern over a much larger data sample than described here. The cloud diameter, D, corresponds to an east-west dimension of the cyclonic cloud pattern, while the amplitude, A, is a dimension from the cloud vortex south to the frontal band. Both D and A are estimated from satellite cloud images in Environmental Satellite Imagery, using procedures described by the authors. These variables were included as standards to which correlations of other variables could be compared for this smaller data sample. All correlations were stratified by whether the cyclones occurred in the

19

Atlantic or Pacific ocean. Table 4 indicates correlations for the years
1975 and 1976 separately.

TABLE 4. Correlation of cloud variables
and the amplitude (Z) of the 500 mb shortwave trough

Data	Z·Lat	Z·D	Z·A	Z·d sinʰ	Z·C (T$_0$=240°K)
Atlantic (1975-14 images)	.89	.33	.47	.63	.63
Atlantic (1976-11 images)	-.50	.50	-.41	-.18	.72
Pacific (1975-21 images)	-.01	.08	.38	-.32	.11
Pacific (1976-12 images)	.10	.22	.32	.02	-.31

The regional and yearly differences are substantial. Initially, it was
intended to use relationships found from correlations in 1975 to develop a
model for specifying shortwave trough amplitude. The model would then be
verified using cloud patterns from 1976. However, the regional and yearly
differences are so marked that the formulation of a general linear model
was not possible.

Differences in correlation between variables can occur because of
phase differences of these variables with time. Since most of our images
are time sequences characterizing the growth cycles of individual storms,
it is possible to analyze differences in the phase of the two variables.
Figure 18 is a time composite of d·sinʰ and C with respect to the time of
maximum trough amplitude (t_m). In the Atlantic, the concentricity as given
by the d-number is in phase with the trough minima; but in the Pacific, the
maximum d-number occurs approximately 24 hours prior to the trough minima.
In the Pacific, for each of the five storm sequences analyzed, the maximum
d-number occurs prior to maximum trough development. In the Atlantic, the
maximum concentricity occurs first only two out of five times. If concen-
tricity is a precursor of trough development in the Pacific, then this
variable might be useful for prognostic purposes. However, it does not
seem to be useful by itself as a single variable for classifying a storm on
a real-time basis.

20

An alternative explanation of differences in the correlations may be caused by the difference in observational coverage between the Atlantic and Pacific oceans. The growth cycle of Pacific storms occurs in regions of poor data coverage and maturity occurs near land where upper air data are present. In regions of missing data, most techniques of data interpolation are conservative when specifying the initial fields. Thus, in remote areas, the amplitude of troughs is likely to be underestimated. If this is the case, then the NEPRF height field used here for correlation is likely to reflect the same systematic behavior. Under these circumstances, the use of objective concentricity to help specify in-phase trough development would be very useful indeed.

2. Relation of major axis to storm movement. Figures 19 and 20 show the major axis of concentricity for four storm sequences in the Pacific and two storm sequences in the Atlantic. Included on these diagrams is the trough axis indicated by a subjective analysis of curvature in the cloud bands to the south of the vortex center. Much of the time, there appears to be a correspondence between the axis of the trough and the major axis. Other times, the axes are systematically displaced from one another by a fixed amount. The axis of concentricity primarily reflects the tight curvature of the cloud bands to the north of the cloud vortex, and, therefore, need not correspond to the trough axis. Table 5 indicates the preference of storm movement as a function of orientation of the major axis. When the orientation of the axis is between 150-180° and 0-30°, there is a high probability that the storm will move east or southeast. If the major axis is within 60° of east (30-150°), the storm will very likely move to the northeast.

TABLE 5. Distribution of twelve-hour storm trajectories as a function of preceding orientation of the major axis

12-hour Storm Movement	Major Axis Orientation					
	180 to 150°	150 to 120°	120 to 90°	90 to 60°	60 to 30°	30 to 0°
Northeast	2	5	2	1	5	2
East	7	0	1	0	1	2
Southeast	7	1	0	1	0	6

21

3. **Locating the storm center.** Extra-tropical storms are less circular than tropical storms and have a less distinctive center of curvature distribution. The ratio of the standard deviations of variability along the axes characterizing the center of the curvature distribution is a measure of the ellipticity, II-B-4, and the d-number is an objective measure of concentricity. Both parameters are useful for classifying the error in objectively locating the center of extra-tropical storms. The average difference between the subjective and objective storm centers is given in Table 6 as a function of these two variables

TABLE 6. Objective and subjective storm center differences (x22 km)
(Numbers in parenthesis are the number of images examined)

Ellipticity (σ_a/σ_b)	d-number		
	0-1.25	1.26-2.50	2.50
1.0-1.5	9(18)	8(8)	1(4)
1.5-2.0	15(17)	8(7)	

A relatively poor center (15x22=330 km) is found when the d-number is small and the ellipticity is high. Conversely, a very good center is found when the d-number is large and the storm is nearly circular (1x22=22 km). Increasing the resolution of the basic cloud pattern image data would decrease these errors.

V. SUMMARY AND CONCLUSIONS

→ This study tests previously developed techniques —

Techniques that have previously been developed for monitoring the intensity, location, and rotation of cyclonic storms from digital satellite cloud patterns are tested in this study for a sample of 83 tropical and 59 extra-tropical cyclone images. The computer programs are designed to produce a normalized distribution of centers of curvature for concentric clouds bands surrounding a storm. The location of the maximum of this distribution is used as a measure of storm position. The horizontally integrated magnitude of the distribution, the d-number, is used as a measure of storm intensity, and the major axis of the distribution is used as a reference line to measure storm rotation.

A. TROPICAL STORMS

For western Pacific typhoons, the cyclone image d-number was used with an area cloudiness parameter to formulate an objective intensity parameter comparable to the Dvorak T-number. The T-number is currently used operationally to describe storm intensity from satellite cloud patterns. A portion of the sample images was used to construct a statistical model of T-number variability using parameters computed from visual and IR images. The model appears to describe the primary time variations of intensity characterizing the growth cycle of tropical storms. In terms of absolute accuracy, the difference between the model and subjective T-numbers is approximately ± 1.0. Corresponding accuracy of T-numbers by analysts is approximately $\pm .5$. To improve the statistical model, recommendations are made to add terms to account for systematic differences between the model and observed T-numbers.

The rotation of the major axis of concentricity of the storm appears to be correlated with direction changes of the storm's trajectory. Generally, anticyclonic (cyclonic) changes in rotation of the major axis occur concurrently with anticyclonic (cyclonic) changes in storm direction. For one typhoon, Polly, it appeared that the rotation may have preceded the subsequent direction changes of the storm's trajectory. The major axis may be useful for diagnosing the movement of erratic storms where a large-scale steering flow is not well defined.

23

The objective tropical storm center compares favorably to the storm position specified by the analyst for storms of strong concentricity. For storms with few concentric bands, the analyst can position the storm more accurately. An improvement in the resolution of the satellite data analyzed here (11 km) will improve the accuracy of the objective technique.

B. EXTRA-TROPICAL STORMS

The relationship between concentric storm properties of extra-tropical storms and the 500 mb height pattern was much less distinct. Regional and yearly differences in correlations between cloud parameters and the amplitude of the 500 mb shortwave trough were substantial and prevented any model development.

In a diagnostic investigation of the regional differences of correlations, it was found that for storms in the Pacific the maximum concentricity (d-number) precedes the development of the trough. In the Atlantic, the tendency was for the maximum d-number to occur simultaneously with trough development.

The major axis of concentricity of extra-tropical cloud patterns appears to generally reflect the curvature of the cloud bands to the north of the cloud vortex. Often this axis is coincident with the axis of the trough as seen by a subjective analysis of curvature in the cloud bands to the south of the cloud vortex. A tendency is noted for storms to move southeast or east if the major axis is within $\pm 30^\circ$ of south. If the major axis is oriented $\pm 60^\circ$ of east, the storm will very likely move northeastward in the next 12-hour period.

Finally, an evaluation of objective storm position was made for extra-tropical storms. The accuracy of cloud vortex position is dependent on the circularity of the storm and the d-number. Extra-tropical storms cannot be objectively positioned as accurately as tropical storms.

C. RECOMMENDATIONS

The most promising application of the above objective techniques is for the analysis of the intensity and rotation of tropical storms. The results described in this report are based on DMSP film images of tropical storms

24

which were then digitized. There are problems in calibrating the various types of IR images in terms of temperature. The regression coefficients used in the storm intensity model and the threshold value of temperature used in defining percentage cloudiness may not be applicable to another data set. A technique to calibrate IR brightness between satellites, perhaps based on sea surface temperature, should be developed. Any operational application of the above technique will be performed on precalibrated digital image data. Therefore, additional model development and subsequent verification should be performed on such precalibrated digital data before eventual application. The techniques developed here with photographic data should be verified with direct digital data.

References

Annual Typhoon Report, 1973 and 1974. Fleet Weather Central/Joint Typhoon Warning Center, Guam, Marianna Islands.

Dartt, D. G., 1976: A pilot analysis of the curvature of extratropical storms. Final Report, Contract N00228-75-C-2363, for U.S. Navy, NEPRF by Control Data Corporation, Minneapolis, MN, 21 p.

Dartt, D. G., 1975: Objective tropical storm parameters from satellite cloud patterns. Tech. Report No. 1, Contract N00228-75-C-2363, for U.S. Navy, NEPRF by Control Data Corporation, Minneapolis, MN, 23 p.

Dartt, D. G., M. S. Ulstad and R. A. Weinberg, 1974: Objective methods for locating the center of tropical storms. Tech. Report No. 1, Contract N66856-3029-5500, for U.S. Navy, NEPRF by Control Data Corporation, Minneapolis, MN, 16 p.

Defense Meteorological Satellite Program (DMSP) User's Guide, 1974. Headquarters Air Weather Service, Scott AFB, Illinois.

Dvorak, V. F., 1975: Tropical cyclone intensity analysis and forecasting from satellite imagery. Mon. Wea. Rev., 103, 420-430.

Environmental Satellite Imagery, February and March 1975, March and April 1976. National Environmental Satellite Service, Washington D.C.

Fett, R. W. and S. Brand, 1975: Tropical cyclone movement forecasts based on observations from satellites. J. Appl. Meteor., 14, 452-465.

Holl, M. M., 1963: Scale and pattern spectra and decompositions. Technical Memorandum No. 3, Contract N228-(62271) 60550 by Meteorology International Inc., Monterey, California.

Nagle, R. E. and C. M. Hayden, 1971: The use of satellite-observed cloud patterns in Northern Hemisphere 500 mb numerical analysis. NOAA Tech. Report NESS 55, U.S. Department of Commerce, Washington D.C.

Sheets, R. C. and P. Grieman, 1975: An evaluation of the accuracy of tropical cyclone intensities and locations determined from satellite pictures. NOAA Tech. Memorandum ERL WMPO-20, U.S. Department of Commerce, Boulder, Colorado.

References (continued)

Troup, A. J. and N. A. Streten, 1972: Satellite-observed Southern Hemisphere
cloud vortices in relation to conventional observations. J. Appl. Meteor.,
11, 909-917
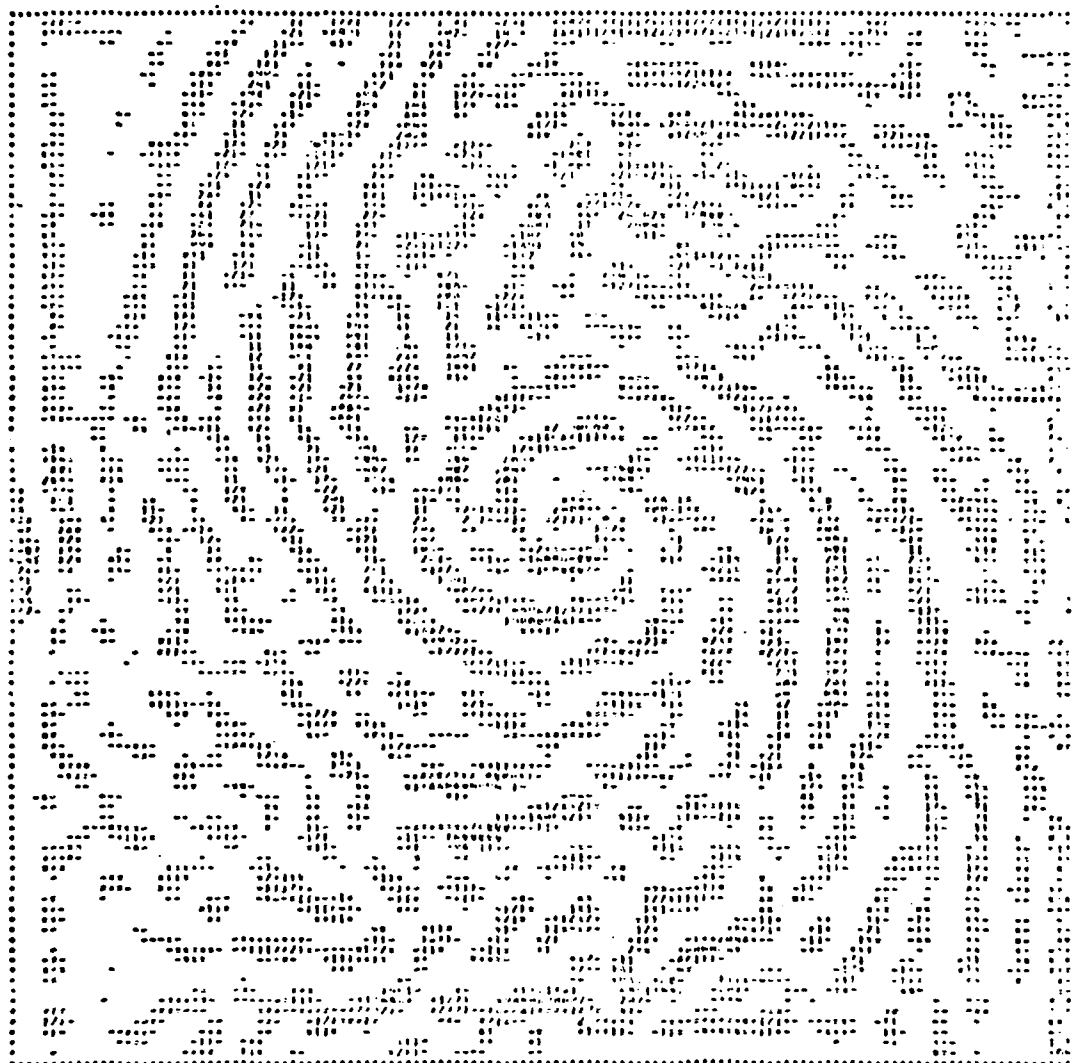
Figure 2. Typhoon Gilda IR filter pattern 04 July, 1226Z.
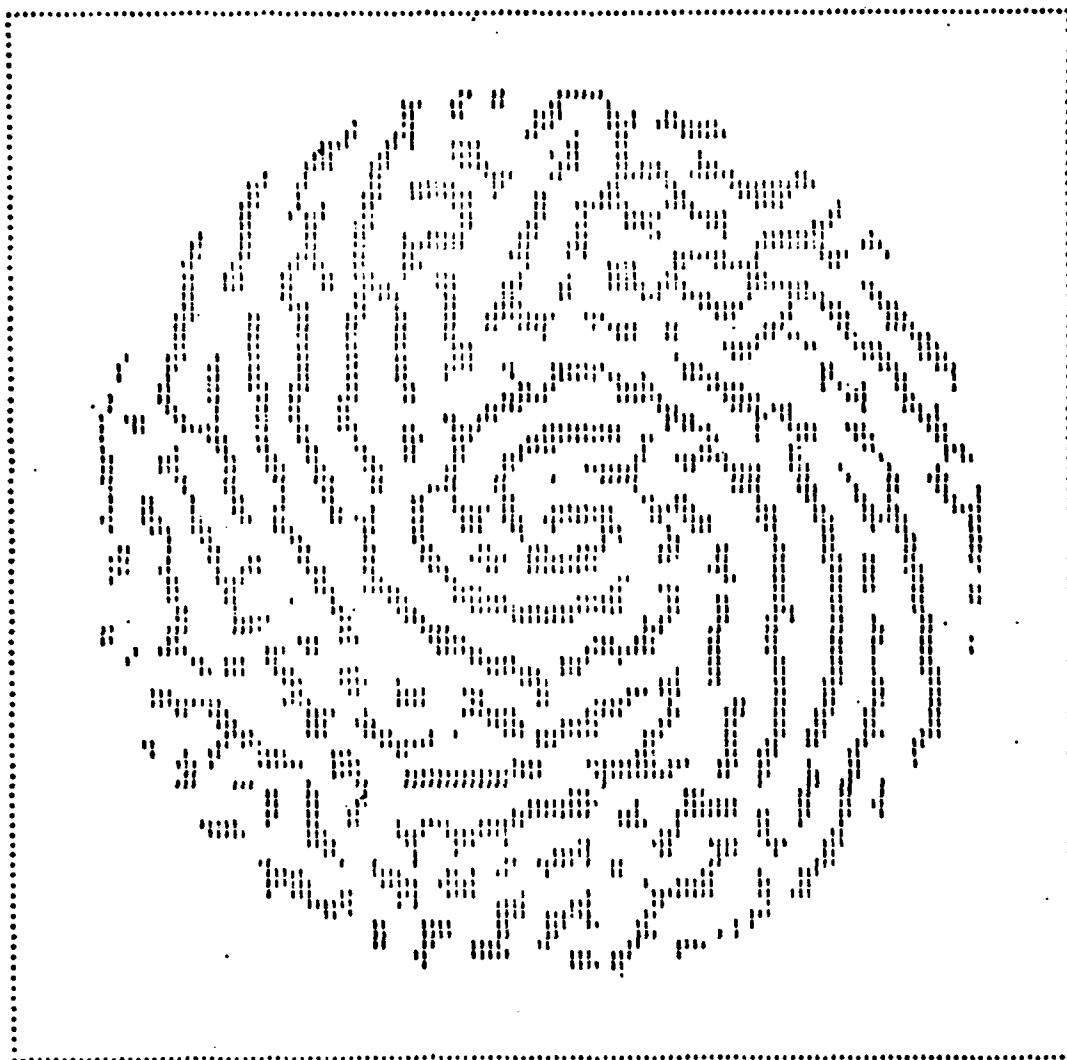
Figure 3.   Typhoon Gilda IR skeleton pattern 04 July, 1226Z.

d=3.2 rays/cell
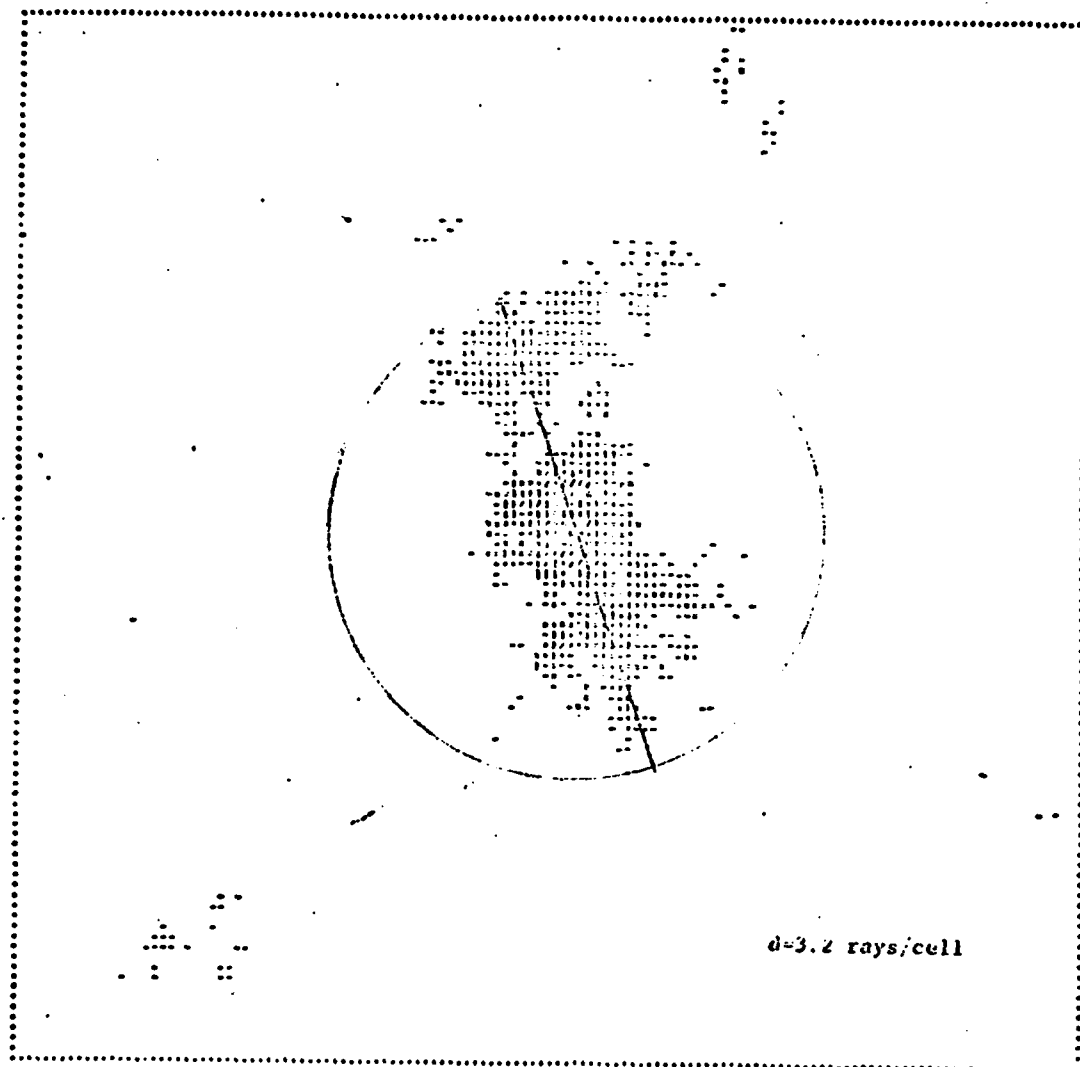
Figure 4.   Typhoon Gilda IR center of curvature pattern 04 July, 1226Z.
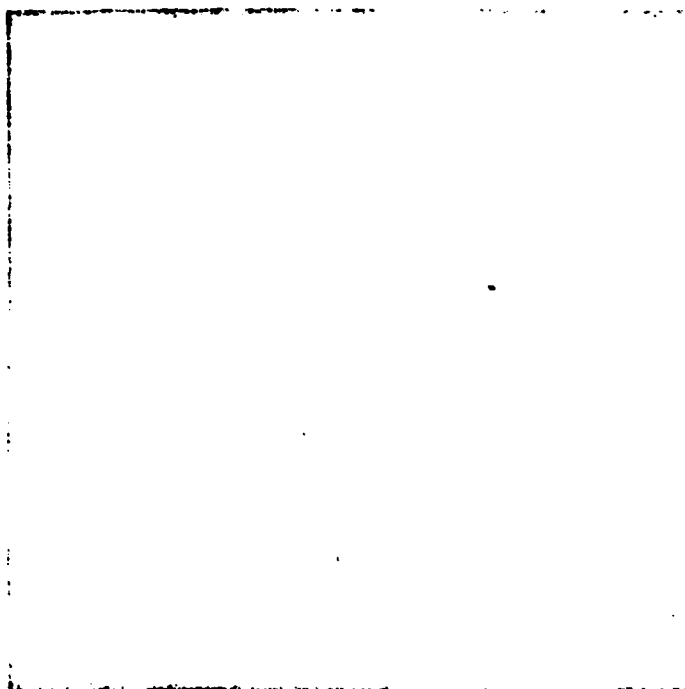
Guam inverted IR normal   Fuchu IR inverse
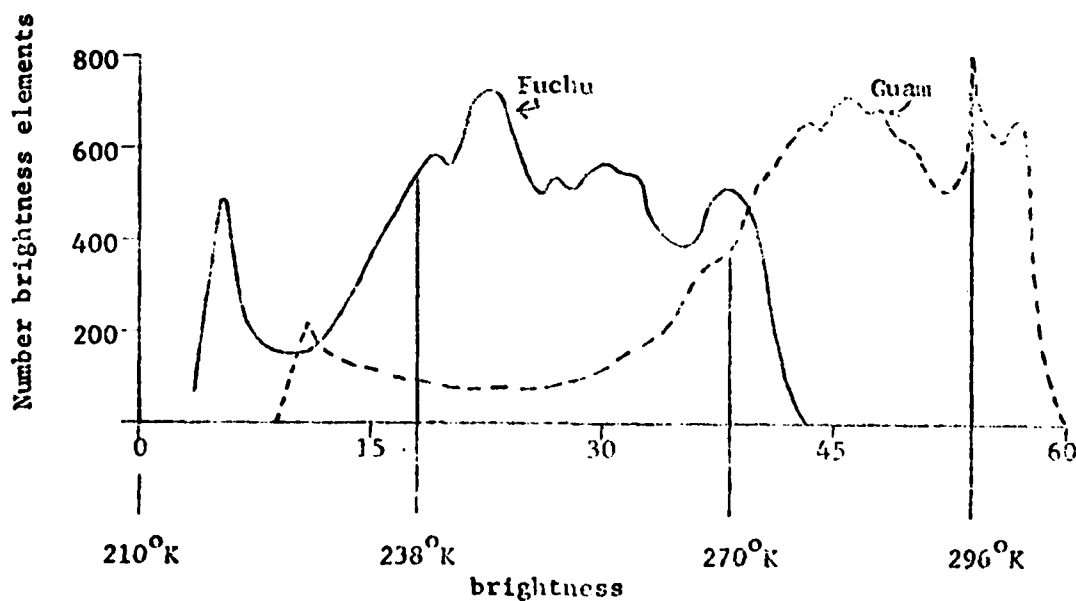
Figure 5.   DMSP IR images for Typhoon Shirley, Sep 4, 1974 (1210Z) from
Guam and Fuchu sites and the respective IR brightness distribu-
tion of each image.
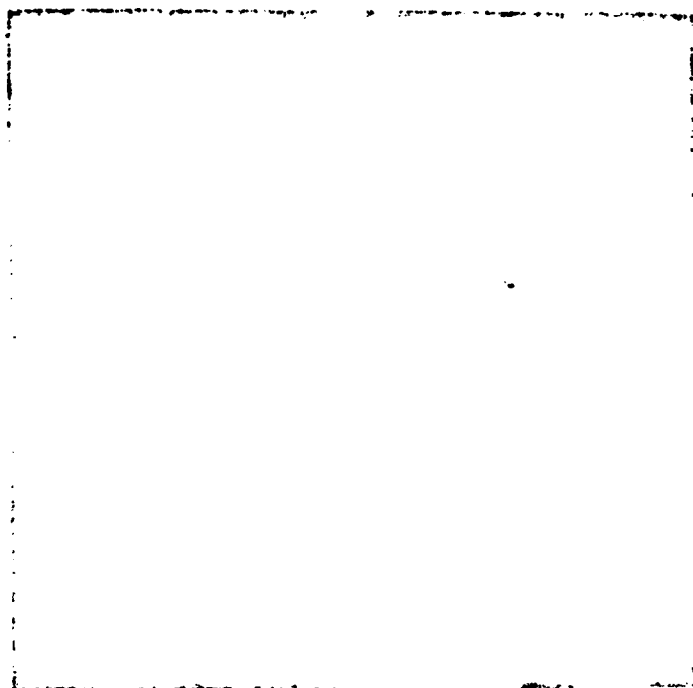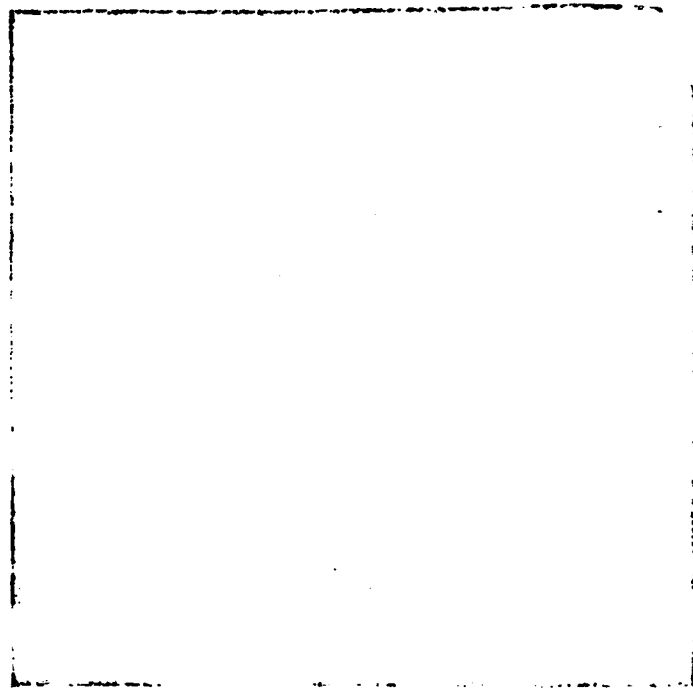
(a) Typhoon Nora   (b) Typhoon Mary
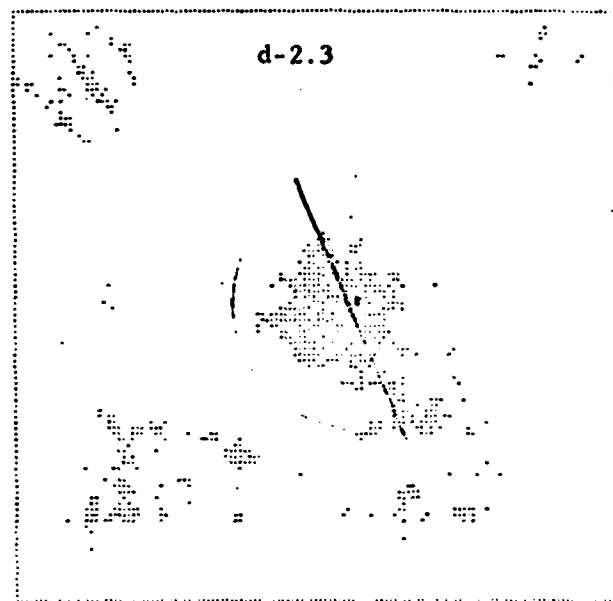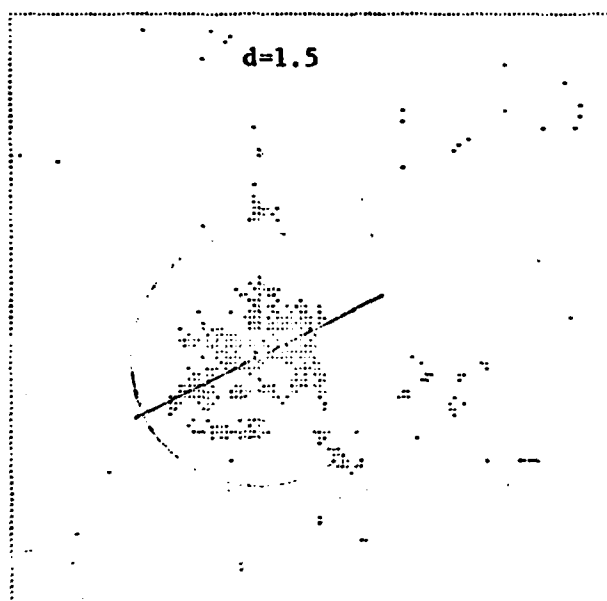
Figure 6.   Images and center of curvature distributions for (a) Typhoon
            Nora, Oct 5, 1973 (2312Z) - visual image and (b) Typhoon Mary,
            Aug 12, 1974 (2143Z) - IR image.
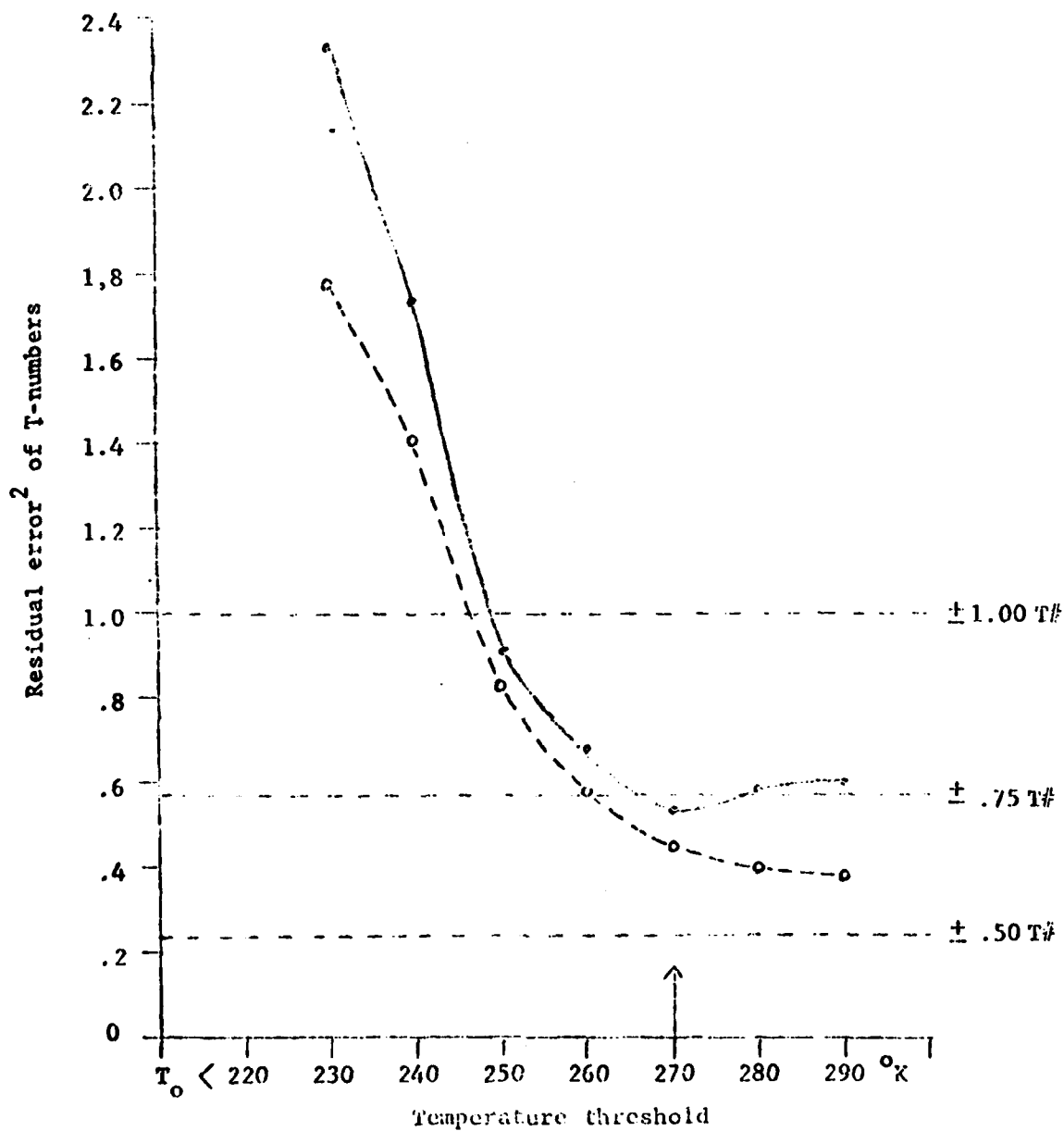
Figure 7. Residual error of statistical model as a function of temperature threshold, T_o, for defining percentage cloudiness. Dots indicate the error curve for visual images, circles the error for IR images.
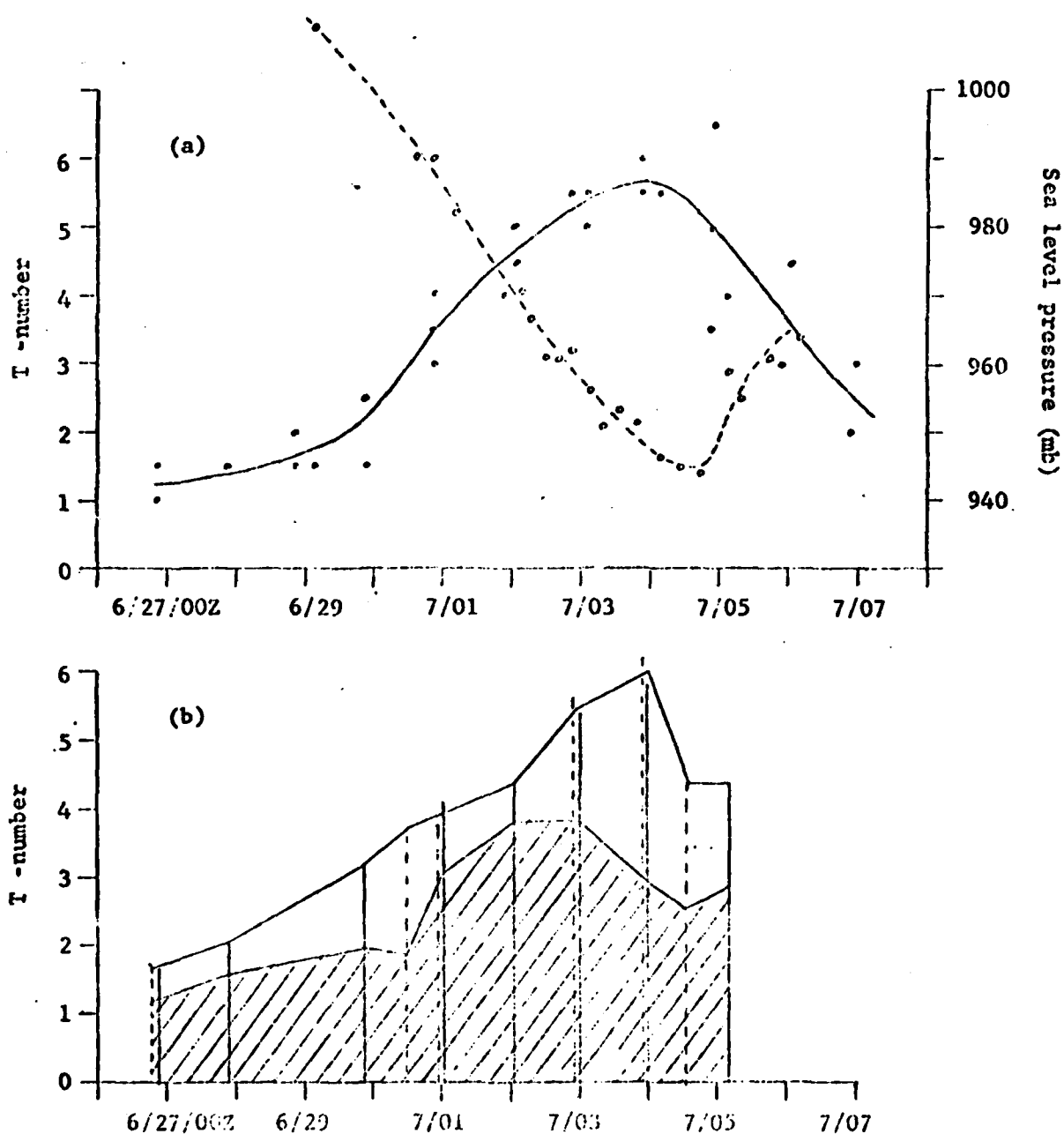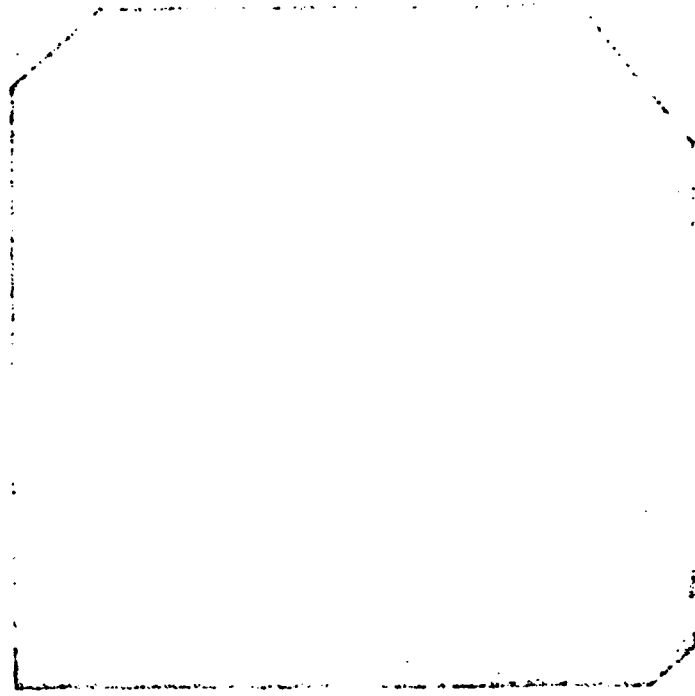
Figure 8. Intensity history of Typhoon Gilda as given by (a) observed T-numbers (dots) and dropsonde surface pressure (circles) and by (b) T-numbers calculated by the model from visual (solid line) and IR (dashed line) images. The shaded area is the contribution to the T-number in the model from the percent cloudiness variable.
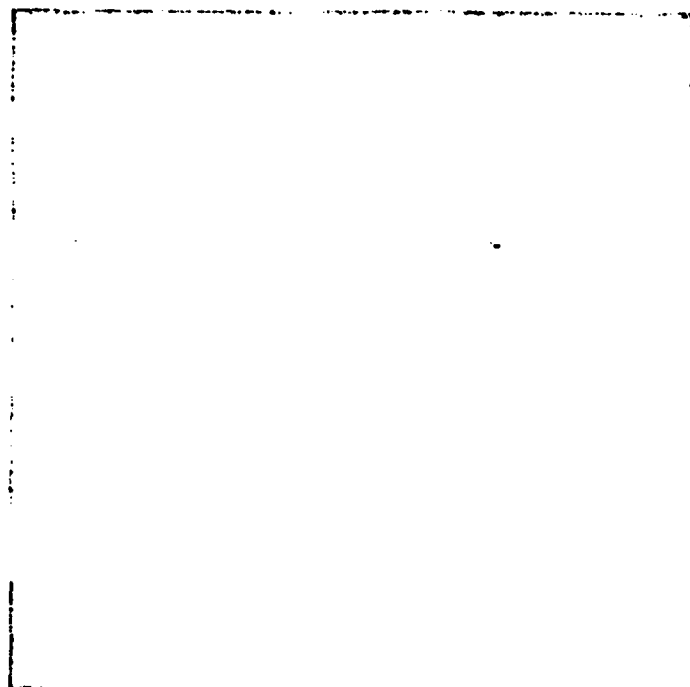
(a) Typhoon Polly   (b) Tropical Storm Rose

d≈3.7   d=.8
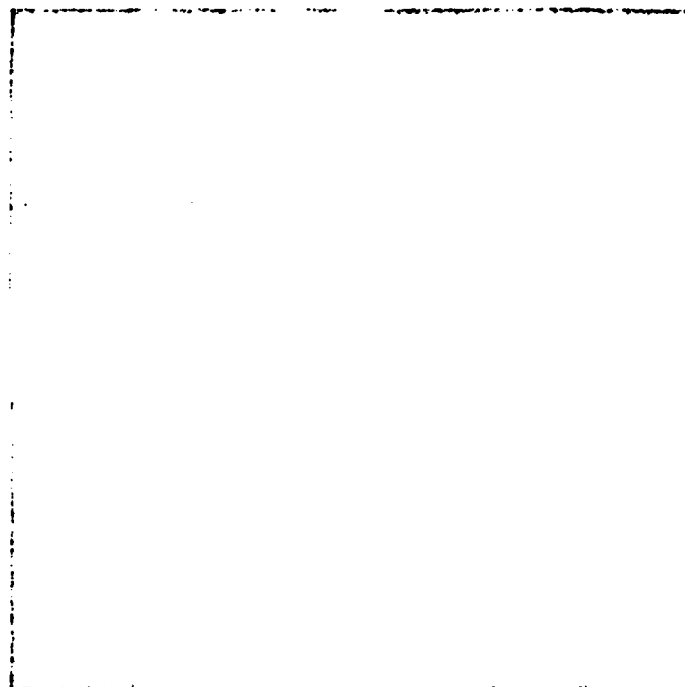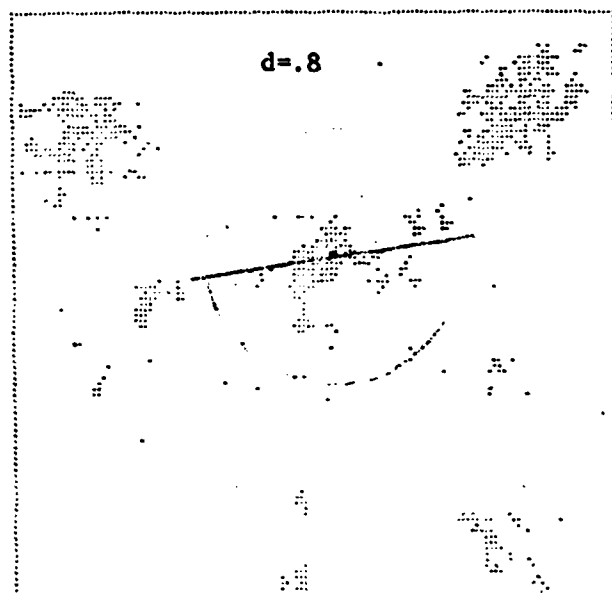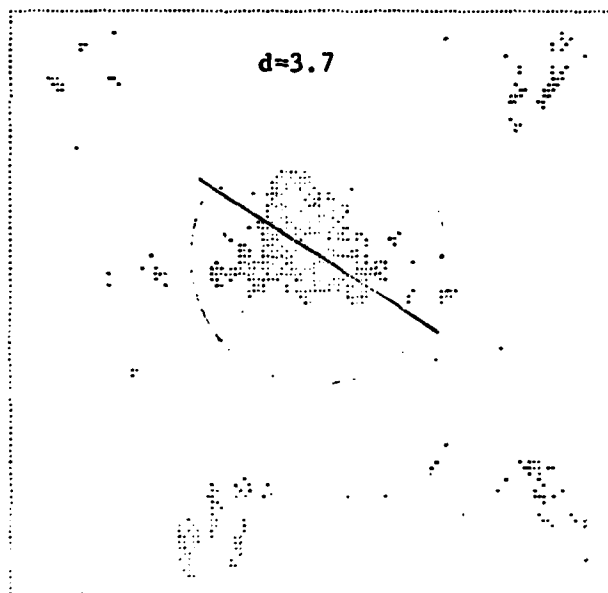
Figure 9.   Infrared images and center of curvature distributions for (a) Typhoon Polly, Aug 30, 1974 (1200Z) and (b) Tropical Storm Rose, Aug 29, 1974 (2318Z).
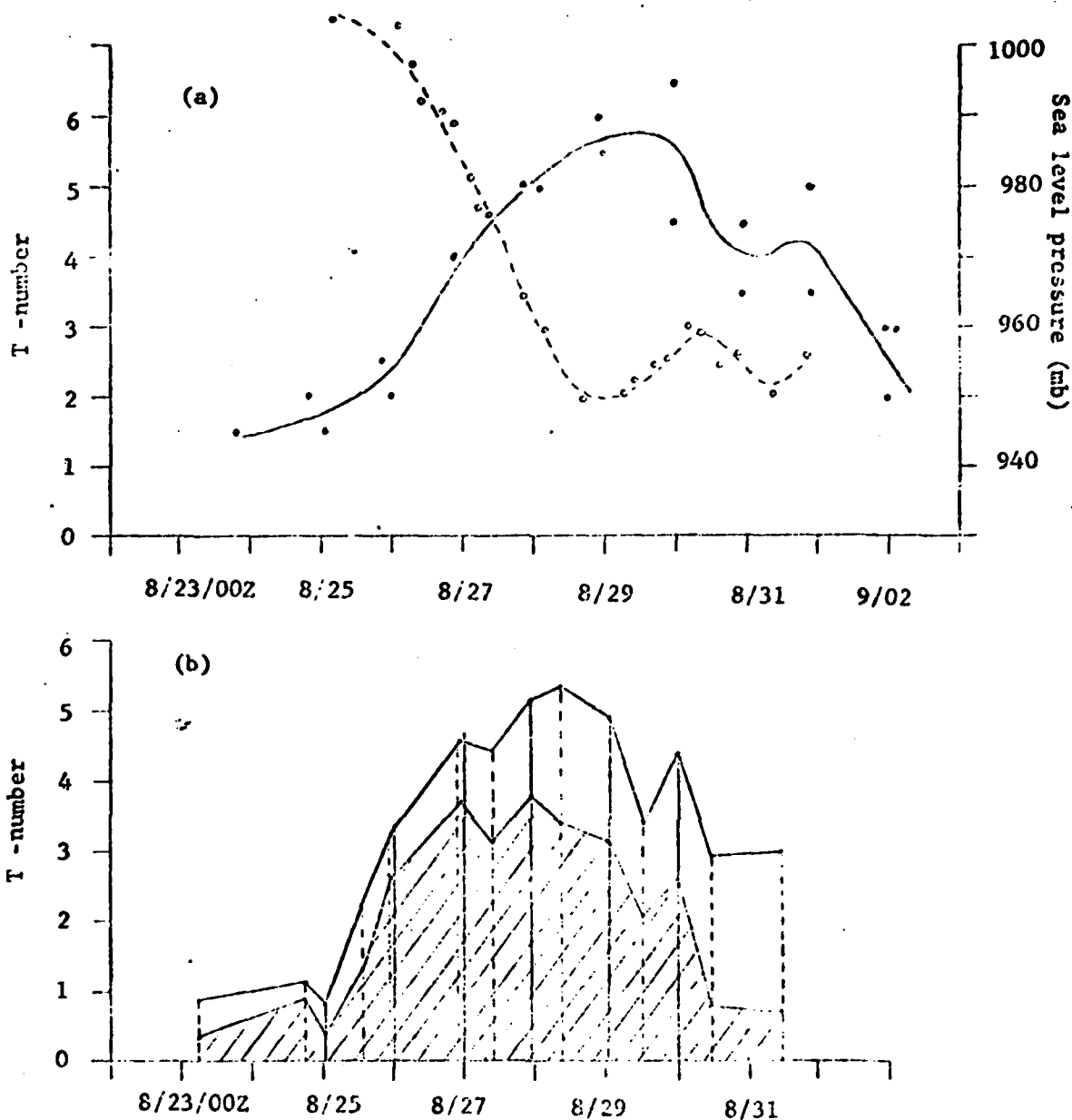
Figure 10. Intensity history of Typhoon Polly as given by (a) observed T-numbers (dots) and dropsonde surface pressure (circles) and by (b) T -numbers calculated by the model from visual (solid line) and IR (dashed line) images. The shaded area is the contribution to the T-number of the model from the percent cloudiness variable.
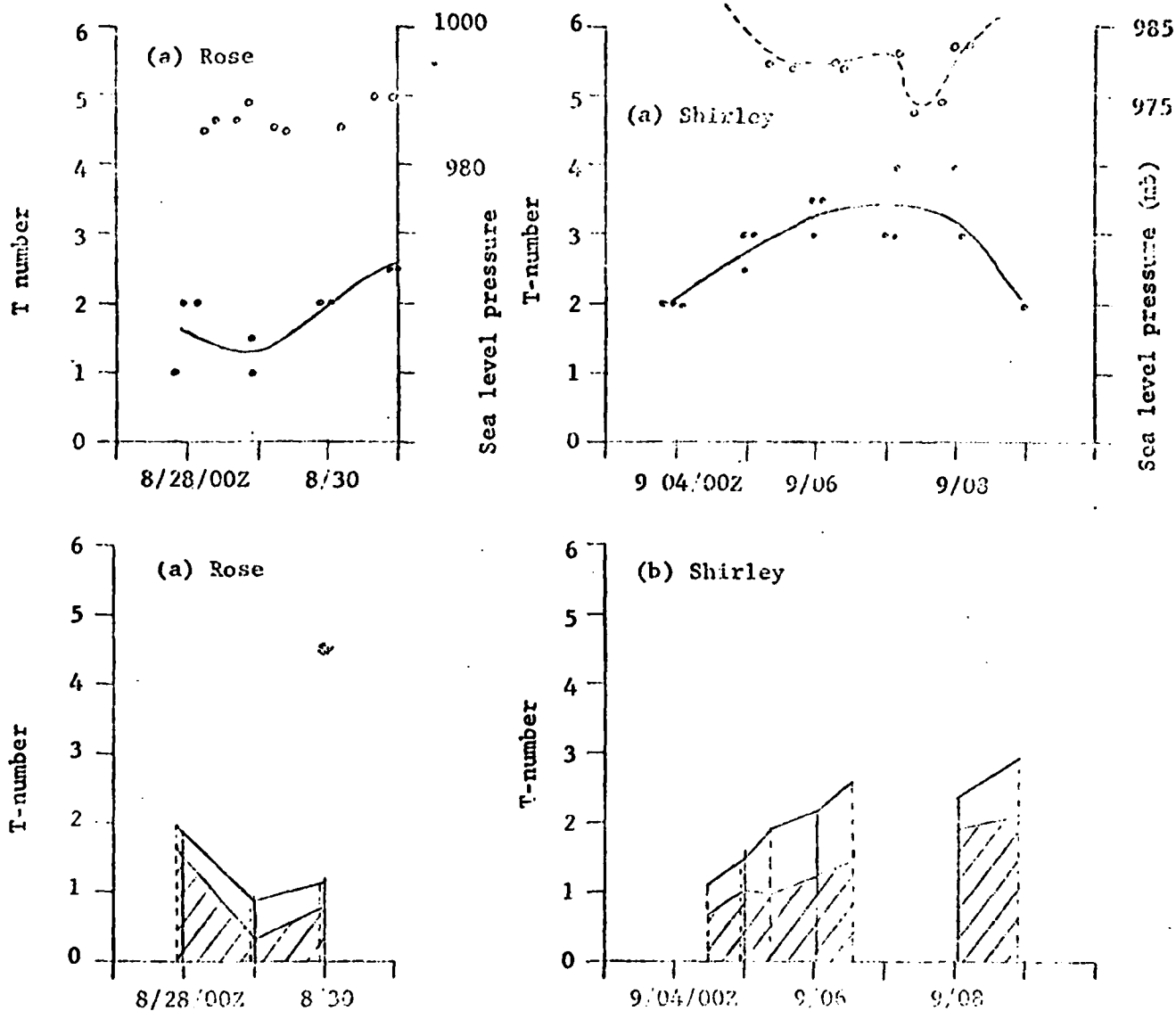
Figure 11. Intensity history of Typhoon Shirley and Tropical Storm Rose as given by (a) observed T-numbers (dots) and dropsonde surface pressure (circles) and by (b) T-numbers calculated by the model from visual (solid line) and IR (dashed line) images. Shaded area is the contribution to the T-number of the model by the percent cloudiness variable.
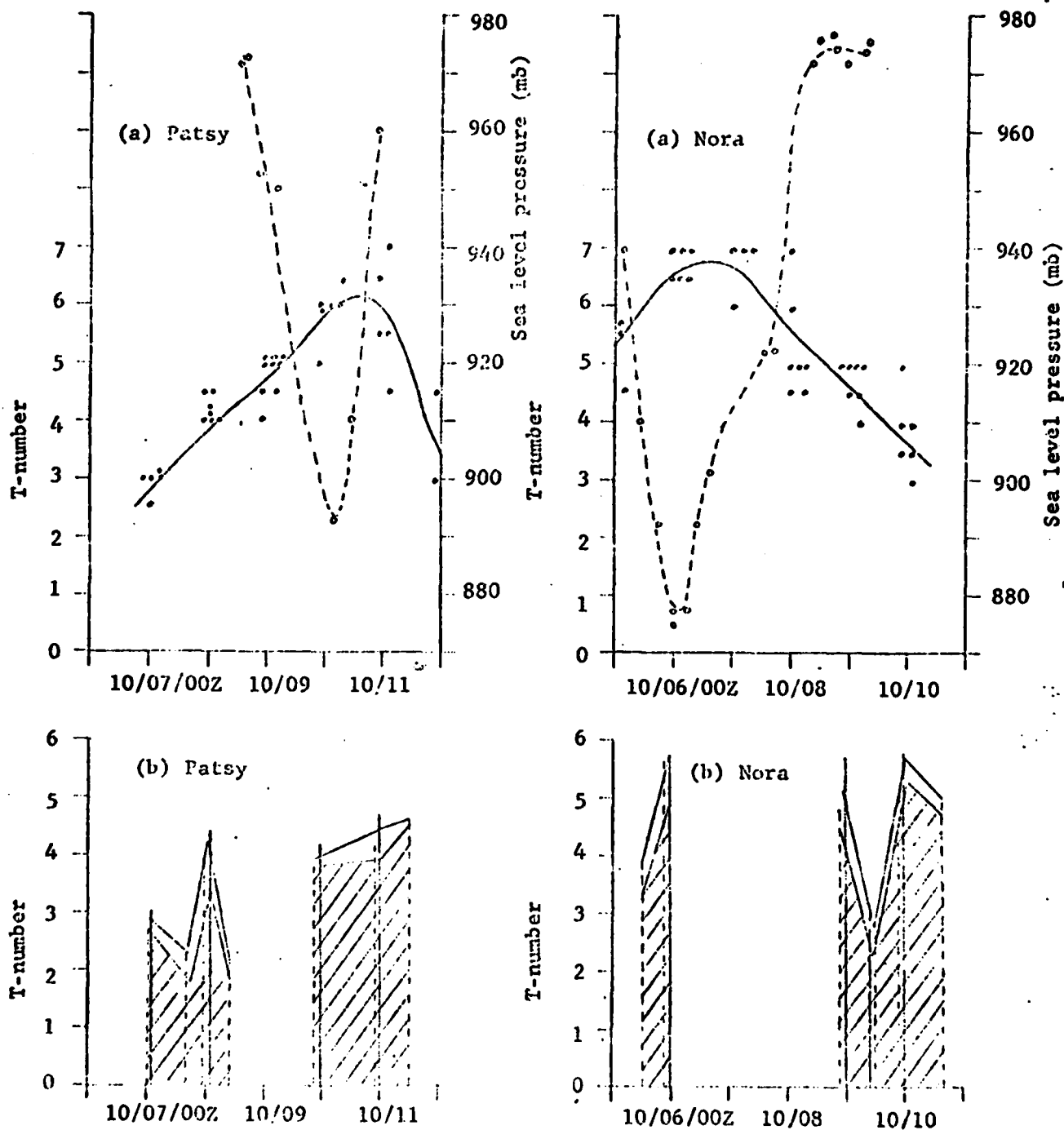
Figure 12. Intensity histories of Typhoons Patsy and Nora as given by (a) observed T-numbers (dots) and dropsonde surface pressure (circles) and by (b) T-numbers calculated by the model from visual (solid line) and IR (dashed line) images. Shaded area is the contribution to the T-number of the model by the percent cloudiness variable.
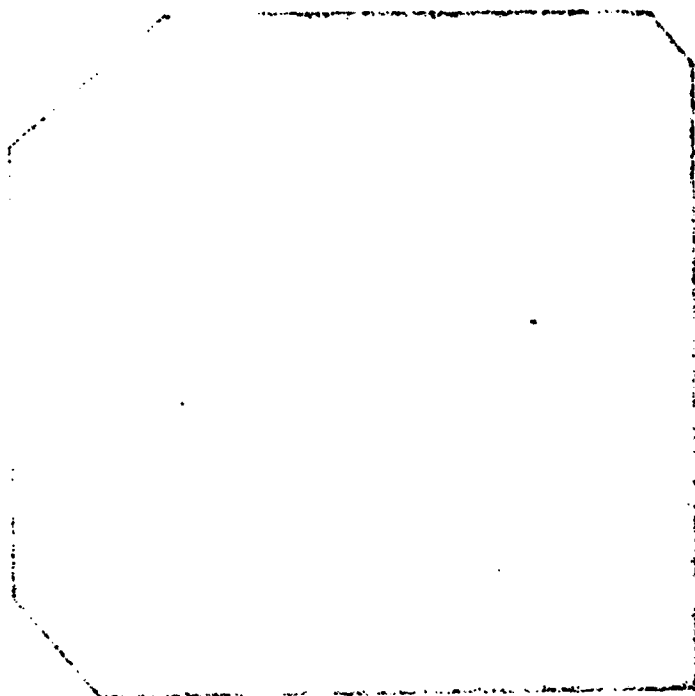
(a) (39N, 143E) March 27 (12Z)   (b) (40N, 150E) March 28 (00Z).

d=.6

d-2.0
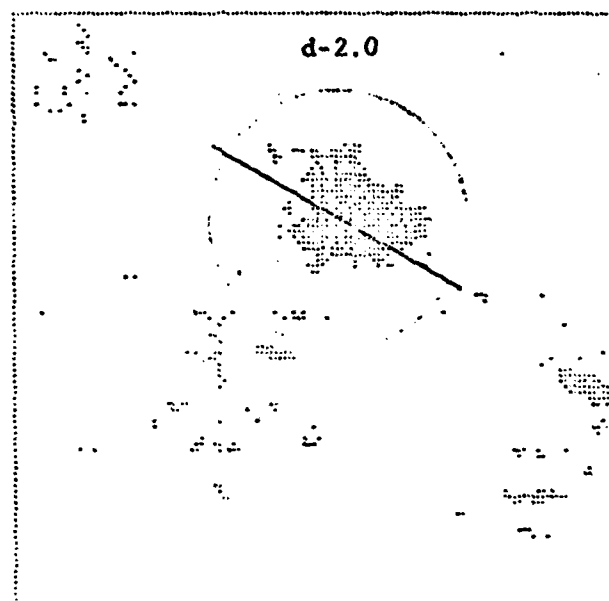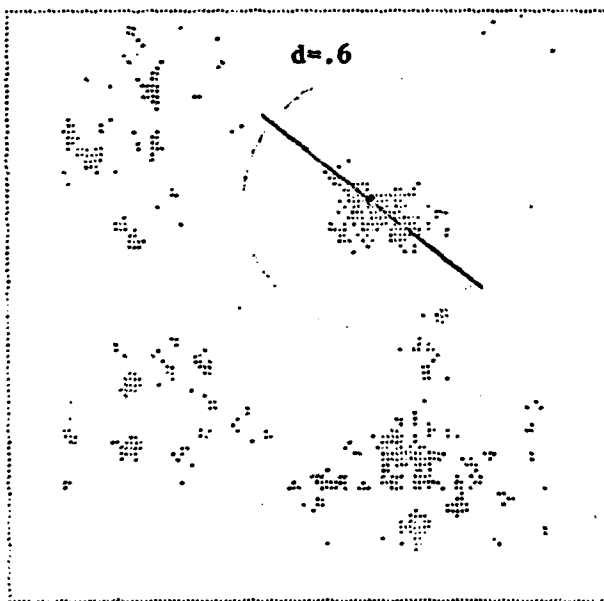
Figure 16. Infrared images and center of curvature distributions for extra-
tropical storm in the western Pacific on (a) March 27, 1976 (12Z)
and (b) March 28, 1976 (00Z).

(a) (43N, 155E) March 28 (11)Z
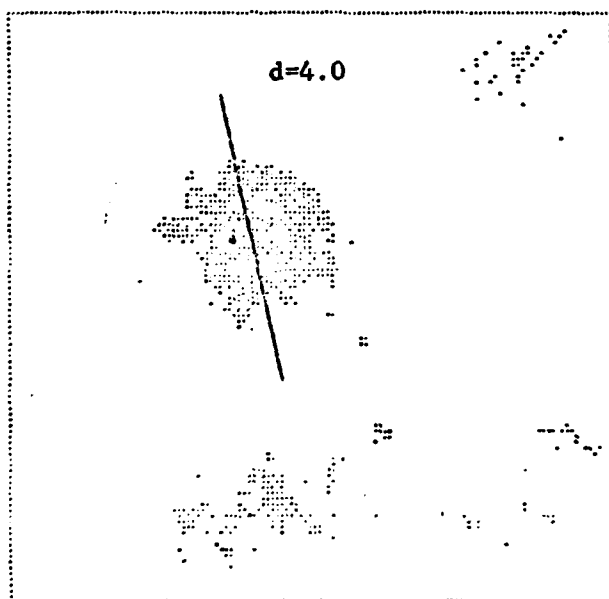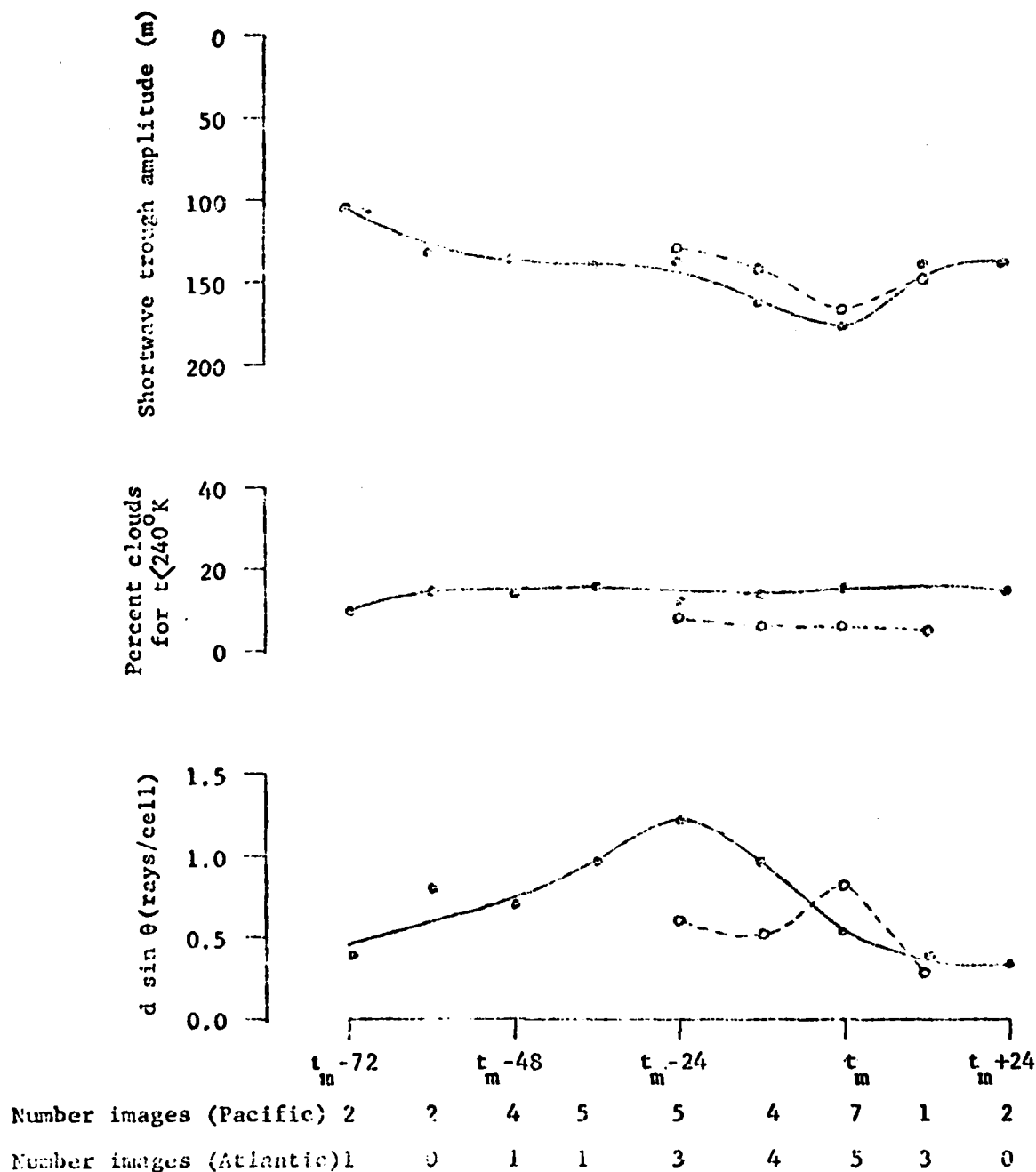
(b) (45N, 160E) March 28 (23Z)

d=4.0

d=4.0
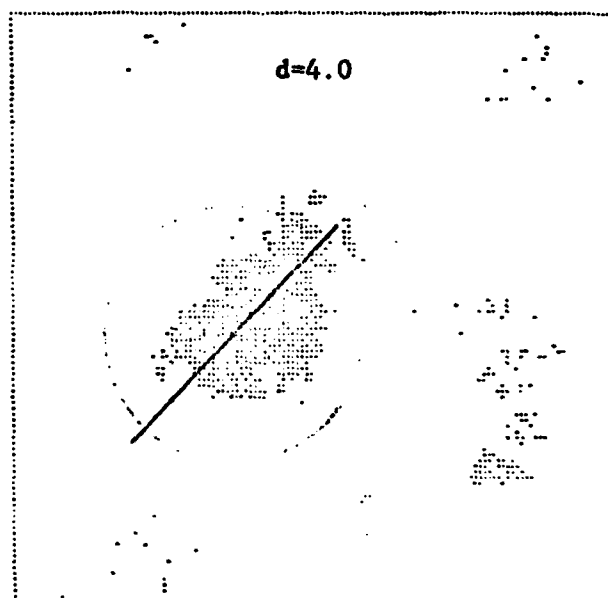
Figure 17.   Infrared images and center of curvature distributions for extra-
tropical storm in western Pacific on (a) March 28, 1976 (11Z) and
(b) March 28, 1976 (23Z).

Figure 18. Time relation of concentricity (d sin θ) and cloudiness to the minimum of the 500 mb shortwave trough. Dots indicate variables for storms in the Pacific; circles indicate variables for storms in the Atlantic. The time of trough minimum is t_m.
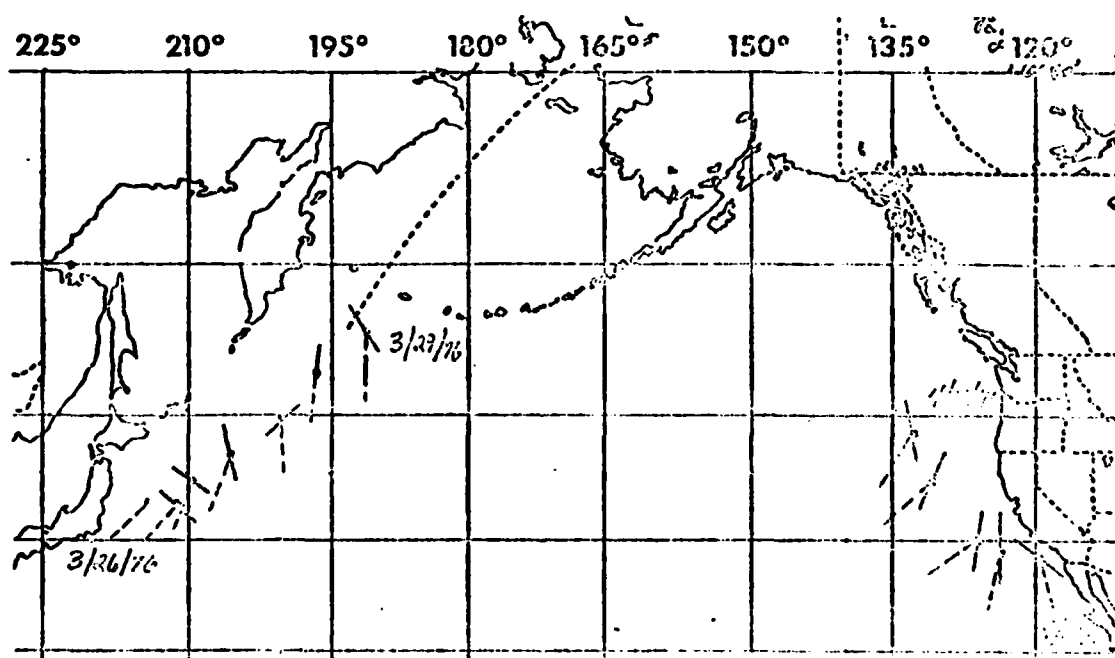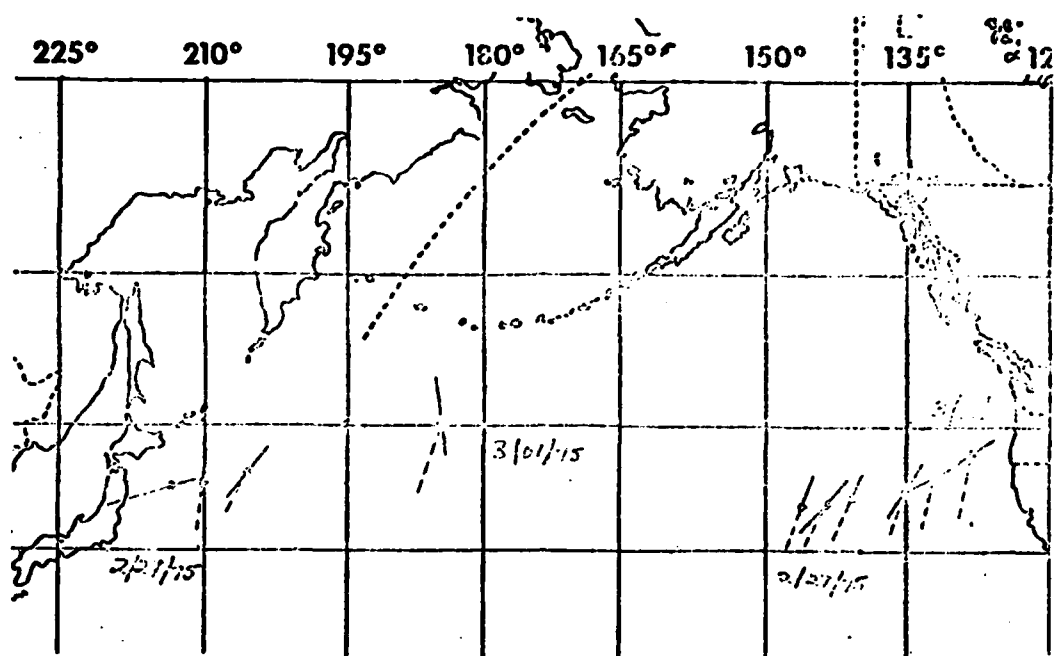
Figure 19. Behavior of the major axis of concentricity (solid line) and upper level trough (dashed line) for four spring storms in the Pacific during 1975 and 1976.
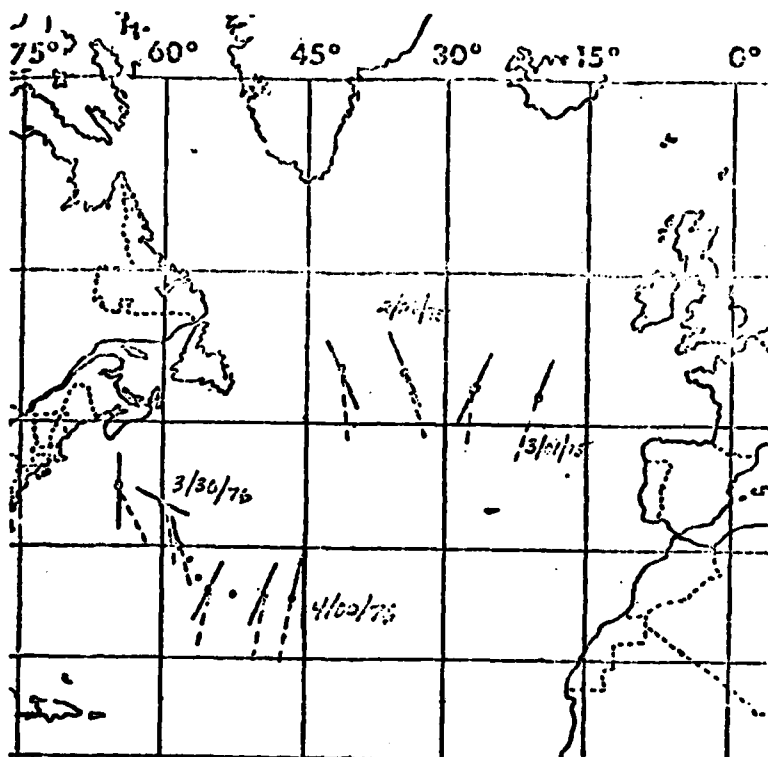
Figure 20.   Behavior of the major axis of concentricity (solid line) and
upper level trough (dashed line) for two spring storms in the
Atlantic during 1975 and 1976.

END

FILMED

5-86

DTIC